The Astrophysical Journal, 940:181 (13pp), 2022 December 1 https://doi.org/10.3847/1538-4357/ac9df5

Measuring He I Stark Line Shapes in the Laboratory to Examine Differences in Photometric and Spectroscopic DB White Dwarf Masses

M.-A. Schaeuble[1,2], T. Nagayama[1], J. E. Bailey[1], M. A. Gigosos[3], R. Florido[4], S. Blouin[5], T. A. Gomez[1], B. Dunlap[2], M. H. Montgomery[2], and D. E. Winget[2]
[1] Sandia National Laboratories, Albuquerque, NM 87185, USA; mschaeu@sandia.gov
[2] Department of Astronomy and McDonald Observatory, The University of Texas at Austin, Austin, TX 78712, USA
[3] Departamento de Física Teórica, Atómica y Óptica, Universidad de Valladolid, E-47071 Valladolid, Spain
[4] iUNAT-Departmento de Física, Universidad de Las Palmas de Gran Canaria, E-35017 Las Palmas de Gran Canaria, Spain
[5] Department of Physics & Astronomy, University of Victoria, Victoria, BC V8P 5C2, Canada
Received 2022 July 27; revised 2022 October 4; accepted 2022 October 25; published 2022 December 5

Abstract

Accurate helium White Dwarf (DB) masses are critical for understanding the star's evolution. DB masses derived from the spectroscopic and photometric methods are inconsistent. Photometric masses agree better with currently accepted DB evolutionary theories and are mostly consistent across a large range of surface temperatures. Spectroscopic masses rely on untested He I Stark line-shape and Van der Waals broadening predictions, show unexpected surface temperature trends, and are thus viewed as less reliable. To test this conclusion, we present in this paper detailed He I Stark line-shape measurements at conditions relevant to DB atmospheres ($T_{\rm electron}$ ≈12,000–17,000 K, $n_{\rm electron} \approx 10^{17}$ cm^{-3}). We use X-rays from Sandia National Laboratories' Z-machine to create a uniform ≈120 mm long hydrogen–helium mixture plasma. Van der Waals broadening is negligible at our experimental conditions, allowing us to measure He I Stark profiles only. Hβ, which has been well-studied in our platform and elsewhere, serves as the n_e diagnostic. We find that He I Stark broadening models used in DB analyses are accurate within errors at tested conditions. It therefore seems unlikely that line-shape models are solely responsible for the observed spectroscopic mass trends. Our results should motivate the WD community to further scrutinize the validity of other spectroscopic and photometric input parameters, like atmospheric structure assumptions and convection corrections. These parameters can significantly change the derived DB mass. Identifying potential weaknesses in any input parameters could further our understanding of DBs, help elucidate their evolutionary origins, and strengthen confidence in both spectroscopic and photometric masses.

Unified Astronomy Thesaurus concepts: White dwarf stars (1799); DB stars (358); Laboratory astrophysics (2004); Atomic physics (2063); Plasma physics (2089)

1. Introduction

White Dwarfs (WDs) are the evolutionary endpoint for ∼98% of all stars. Approximately 20% of all known WDs have helium-dominated atmospheres. Among them, only those showing neutral helium lines are called DBs (Sion et al. 1983; Koester & Kepler 2015). Accurate DB masses are important to multiple areas of astrophysics, including stellar evolution (e.g., Nather et al. 1981; Fontaine & Wesemael 1987; Werner & Herwig 2006), and stellar mass loss processes (e.g., Choi et al. 2016; Cummings et al. 2018). Most DB masses are measured using either the spectroscopic or photometric methods.

The accuracy of the spectroscopic method, which relies on fitting observed spectra with calculations, has been questioned due to uncertain input physics (e.g., Bergeron 1993; Bergeron et al. 2011; Tremblay et al. 2013; Koester & Kepler 2015; Genest-Beaulieu & Bergeron 2019b; Cukanovaite et al. 2021). Atomic line shapes relating the width of an observed line to a stellar surface gravity ($\log g$)/mass are difficult to calculate and are the critical ingredient in the spectroscopic method. Details of all line broadening processes found in DB atmospheres must be included in spectroscopic models. The DB community uses the semi-analytical Beauchamp et al. (1997) line shapes (henceforth called B97) to account for the Stark broadening (caused by charged plasma particles), while the Van der Waals contribution (caused by plasma neutrals) is modeled using the Unsold (1955) and Deridder & van Renspergen (1976) predictions (henceforth called U55 and D76). Tremblay et al. (2020) recently used the computer-simulation approach (e.g., Gigosos et al. 2014) to reinvestigate He I Stark profiles, and the resulting line shapes agreed very well with the B97 calculations. To our knowledge, no laboratory He I Stark line-shape experiments have ever been performed at conditions applicable to DB atmospheres. However, He I full width at half maximum (FWHM) data have been published at electron densities (n_e) higher and lower than those found in DBs (e.g., Chiang et al. 1977; Perez et al. 1991; Büscher et al. 1995; Milosavljević and Djeniže 2002). No experimental data for the Van der Waals broadening models exist at DB atmosphere conditions.

The photometric method, considered simpler and more reliable than the spectroscopic technique, has recently been applied to many DBs due to the release of Gaia parallax measurements (Genest-Beaulieu & Bergeron 2019a, 2019b). This approach combines the parallax data with a fit to the measured stellar flux to arrive at a mass (Tremblay & Cukanovaite 2019). Only DB atmospheric flux calculations, a mass–radius relationship, and a dereddening algorithm are needed as an input. Each of these are thought to be easier to calculate and validate than atomic line shapes. However, as pointed out by Genest-Beaulieu & Bergeron (2019b),

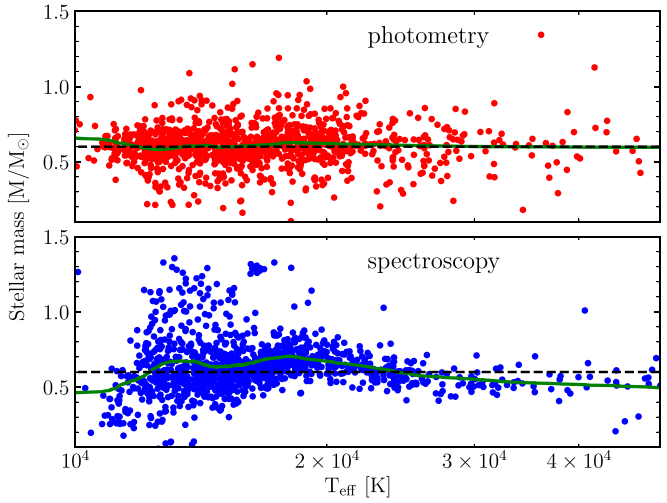

Figure 1. DB mass trends plotted as a function of $T_{\rm eff}$. The top panel shows photometric masses, while the bottom depicts spectroscopic masses. The green line is a moving average fit of the individual data points.The black dotted line at $M/M_\odot = 0.6$ serves as a guide to the reader. All plotted data are taken from Table 1 of Genest-Beaulieu & Bergeron (2019b).

photometric temperatures can be highly sensitive in the $22{,}000\,{\rm K} \lesssim T_{\rm eff} \lesssim 26{,}000\,{\rm K}$ range, where the main opacity source switches from He I bound–free to He II free–free. Furthermore, because the photometric method is heavily dependent on measured parallaxes, large uncertainties in those values lead to large mass uncertainties (Genest-Beaulieu & Bergeron 2019b).

Genest-Beaulieu & Bergeron (2019b) published a detailed investigation of photometric and spectroscopic DB masses. Their results are shown in Figure 1, where the top panel shows photometric DB masses as a function of surface temperature ($T_{\rm eff}$) and the bottom panel depicts the spectroscopic values. We plot a black dotted line at $M/M_\odot = 0.6$ in each panel to guide the reader, along with a moving average fit of the masses (green). The photometric masses exhibit almost no $T_{\rm eff}$ dependency and match the expected mass. Spectroscopic masses, however, show clear $T_{\rm eff}$ trends. At $T_{\rm eff} > 16{,}000\,{\rm K}$, Stark broadening is thought to dominate spectra because the atmospheric plasma contains more charged particles due to a higher ionization fraction compared to cooler temperatures. Weaknesses in the B97 calculations are blamed for the observed mass trends. At $T_{\rm eff} < 16{,}000\,{\rm K}$, Van der Waals broadening is believed to control line broadening, because more neutrals are present in the plasma. The increased scatter in that temperature range is ascribed to deficiencies in the U55 and D76 predictions (e.g., Bergeron et al. 2011; Koester & Kepler 2015; Genest-Beaulieu & Bergeron 2019a, 2019b). The combination of the simpler input physics for photometric method, lack of $T_{\rm eff}$–mass trends, and the agreement with the expected DB mean mass seem to validate the assumption that photometric masses are more reliable than spectroscopic ones.

Developing a deeper understanding of the spectroscopic mass problems is essential to our comprehension of DBs. If it is shown that, contrary to present-day assumptions, spectroscopic mass are reliable, our current understanding of stellar evolution would be incorrect. DBs cool as they age, and the spectroscopic mass trend shown in Figure 1 would indicate that different DB generations have varying masses. Such a finding would counter fundamental tenets of modern stellar evolution and would also invalidate the currently accepted DB evolutionary model. A natural starting point for such an investigation is benchmark laboratory experiments aimed at testing line-shape calculations used in DB atmospheres. If laboratory data do not agree with calculations, the culprit for the spectroscopic mass trends has been identified. However, if line-shape models agree with experiments, other spectroscopic method input parameters, such as atmospheric structure assumptions, may be flawed.

In this paper, we perform validation tests for the B97 Stark model using two strong He I lines found in DB atmospheres: the $3p \rightarrow 2s$ He I line at 5875 Å (henceforth referred to as He5875) and the $3d \rightarrow 2p$ He I line at 5015 Å (henceforth referred to as He5015). The U55 and D76 models predict <0.07 Å Van der Waals broadening at our highest experimental neutral densities ($n_{\rm neutral} \approx 1 \times 10^{18}\,{\rm cm}^{-3}$). The neutral density in our experiments varies by a factor of ≈ 2 and no dependence of line width on $n_{\rm neutral}$ was found, confirming that Van der Waals broadening is insignificant. In $n_{\rm e}$ and electron temperature ($T_{\rm e}$) space, our experiments are performed at DB atmosphere conditions ($T_{\rm e} \approx 12{,}000$–$17{,}000\,{\rm K}$, $n_{\rm e} \approx 10^{17}\,{\rm cm}^{-3}$). For additional insight into He line shapes and their effect on DB masses, we also validate our own, computer-simulation-based line shapes, which represent an improvement and update of those presented in Gigosos et al. (2014). Plasma $T_{\rm e}$, $n_{\rm e}$, and $n_{\rm neutral}$ are diagnosed sufficiently well to qualify for benchmark experiment status.

We find that our experimental line shapes agree with B97 and our own calculations within experimental uncertainties. The DB mass uncertainty associated with our experimental He I $n_{\rm e}$ uncertainties is estimated to be smaller than the spectroscopic-photometric mass differences in the temperature regimes accessed by our validation tests. Our results therefore indicate that perceived weaknesses in Stark predictions may not be responsible for the DB spectroscopic mass discrepancies. Identifying which other spectroscopic input parameters may be responsible for the observed mass trends is difficult. Cukanovaite et al. (2021) showed that small changes in DB atmospheric modeling assumptions can have significant effects on the inferred spectroscopic mass. Other spectroscopic mass inputs such as the assumed atmospheric structure or data analysis methods could also introduce undetected errors. Closer investigation of the latter would have an impact on all WD astrophysics, because these data analysis methods are used for deriving non-DB spectroscopic masses as well (e.g., Dufour et al. 2008; Tremblay et al. 2013). Finally, the photometric method and its sensitivities to the input physics should also be scrutinized further.

This paper is organized as follows: In Section 2, we give an overview of the WDPE platform on Sandia National Laboratories' *Z*-machine. Section 3 describes our data extraction and analysis techniques. The overlap of the plasma conditions reached in our experiment and those found in DBs is discussed in Section 4. Experimental results are presented in Section 5, followed by conclusions in Section 6.

2. The WDPE at SNL's *Z*-machine

Benchmark experimental line-shape data must be collected under conditions that fulfill several key requirements. First, reliable and accurate plasma diagnostics are needed. The He I line-shape data presented in this paper require $T_{\rm e}$, $n_{\rm e}$, and $n_{\rm neutral}$ diagnostics. Second, line-shape data can only be extracted from accurate absorption measurements that are free from any self-emission effects. In this section, we describe the

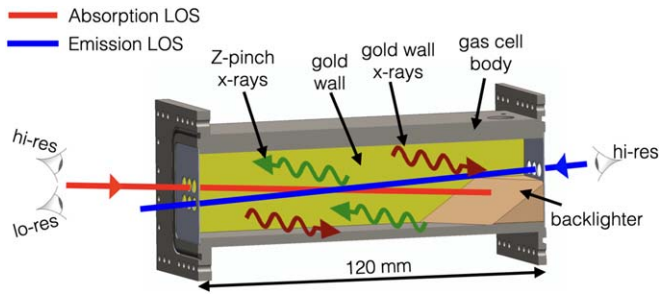

Figure 2. WDPE gas cell cross section. Major hardware components as well as Z-pinch and gold wall photons are identified. The absorption LOS path is given in red and the emission LOS path is plotted in blue.

WDPE platform and demonstrate that it allows us to collect all data needed for a benchmark experiment.

A thorough description of the WDPE platform and our experimental setup is given in Falcon et al. (2013, 2015) and Schaeuble et al. (2019). Recent updates to allow for accurate measurements of He I line shapes are described in Schaeuble et al. (2021). Only a short overview of the WDPE platform is given here.

We perform the WDPE He line-shape validation experiments at the currently most energetic pulsed X-ray source on earth: SNL's *Z*-machine. This pulsed power driver converts a ≈26 MA current into an X-ray drive using a dynamic hohlraum (McDaniel et al. 2002; Bailey et al. 2006; Rose et al. 2010; Jones et al. 2014; Rochau et al. 2014; Sinars et al. 2020). We can use the *Z*-machine X-rays to reproduce a DB atmosphere in the laboratory by filling the 120 mm long WDPE gas cell (see Figure 2) with a H/He gas mixture. Our gas cell is placed ≈324 mm away from the Z-pinch source and designed such that X-rays overfill the cell. This ensures uniform heating of the macroscopic plasma. Z-pinch X-rays (green arrows in Figure 2) traverse the H/He gas mixture cell and deposit their energy into the gold back wall and backlighting surface. The photons reradiated (dark red arrows in Figure 2) from these two hardware pieces then heat the H/He gas mixture and turn it into a plasma.

Due to continuous heating from the gold back wall, the H/He plasma steadily increases in T_e and n_e throughout our experiment (Falcon et al. 2015; Schaeuble et al. 2019). Use of time-resolved spectrometers allows us to collect and test line shapes at multiple plasma parameter values in a single experiment. Gas pressure and composition can be used to control n_e, n_{ion}, and $n_{neutral}$. In DB astronomy, $n_{neutral} = n_{H\,I} + n_{He\,I}$. We adopt the same definition here. At our plasma conditions, hydrogen is the main electron donor while helium largely stays neutral. Plasma $n_{H\,I}$ therefore decreases as a function of time resulting in each experiment covering a range of plasma conditions ($12{,}000\,\mathrm{K} \lessapprox T_e \lessapprox 17{,}000\,\mathrm{K}$, $5\times10^{16}\,\mathrm{cm^{-3}} \lessapprox n_e \lessapprox 5\times10^{17}\,\mathrm{cm^{-3}}$, $5\times10^{17}\,\mathrm{cm^{-3}} \lessapprox n_{neutral} \lessapprox 1\times10^{18}\,\mathrm{cm^{-3}}$). Representative T_e, n_e, and $n_{neutral}$ trends observed during an experiment are shown in Figure 3. T_e is shown in the top panel, n_e is depicted in the center, and $n_{neutral}$ trends are plotted on the bottom. We list the gas mixtures, pressures, average n_e, $n_{neutral}$, and diagnostics setups (discussed below) for all shots considered in this paper in Table 1. The gas fill pressures listed in Table 1 were collected using an in situ piezoresistive pressure sensor attached to the gas cell during the experiment (Falcon 2014; Schaeuble et al. 2021). Extraction methods for each experimental

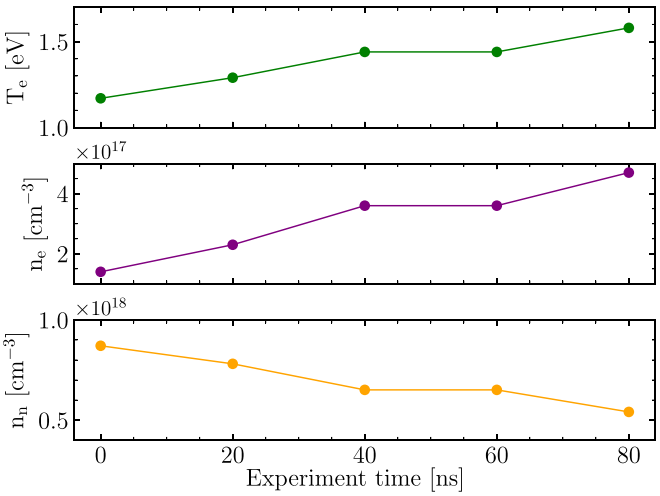

Figure 3. Temporal evolution of T_e (top panel, green) n_e (middle panel, purple), and $n_{neutral}$ (bottom panel, orange) measured for experiment z3195.

parameter plotted in Figure 3 and listed in Table 1 are discussed in Section 3.1.

When using absorption spectra to measure line shapes, it is crucial to ensure that self-emission contamination in the collected data is either negligible or accounted for. WDPE absorption spectra consist of the backlighter spectrum attenuated by the plasma and plasma self-emission processes. If the backlighter is weak, plasma self-emission processes cannot be overcome and the absorption spectrum is thus contaminated and unsuitable for line-shape studies. We collect absorption and emission spectra on each shot, and these enable us to determine the self-emission contamination for the He5015 and He5875 lines. We find that no significant self-emission is present for He5015, while He5875 shows large self-emission effects. We therefore also collect high-resolution He5875 absorption and emission data on CCD spectrometers. These two datasets are calibrated and then subtracted. The He5015 data is processed without performing a self-emission correction. To collect the needed experimental data, the photons emitted from the H/He plasma are transported to two CCD-based and one film-based streaked (i.e., time-resolved) spectrometer system via fiber optics. The absorption line-of-sight (LOS; red in Figure 2) runs along the gold back wall terminating on the backlighter, which is also heated by Z-pinch X-rays. Since the backlighter is hotter than the plasma (backlighter $T \approx 25{,}000$ K, plasma $T \approx 12{,}000$ K), an absorption spectrum results. The emission LOS (blue in Figure 2) also runs along the gold back wall and exits the gas cell. Only emission data are captured on this LOS.

The CCD systems record higher-resolution data ($\lambda/\Delta\lambda \approx 1000$ at 5000 Å) compared to the film system ($\lambda/\Delta\lambda \approx 500$ at 5000 Å). All He I line-shape data presented in this paper are collected on the CCD systems for accurate line-shape testing (Schaeuble et al. 2021). The Hβ line for all our experiments is captured on film, except for shot z3462, during which it was recorded on the CCD. Since the Hβ line is broad and theoretically well-understood, $\lambda/\Delta\lambda \approx 500$ is sufficient to accurately infer n_e from this line. Sample experimental spectra are shown in Figure 4. The top panel shows the spectrum containing Hβ, He5015, He5875, and the He I line at 4713 Å. Analysis of the 4713 Å He I line is beyond the scope of this paper. The relative intensities of the absorption lines shown in

Table 1
Gas Fills, Pressures, Average n_e, $n_{neutral}$, and Diagnostics Setups for the WDPE Shots Considered in This Paper

Shot #	Gas press. (Torr)	Gas fill [% H_2:% He]	$\langle n_e \rangle$ (cm^{-3})	$\langle n_{neutral} \rangle$ (cm^{-3})	Hβ System	He5015 System	He5875 System
z3195	20.71	50:50	3.1×10^{17}	7.0×10^{17}	film	···	CCD
z3402	22.17	50:50	1.8×10^{17}	9.0×10^{17}	film	···	CCD
z3403	16.84	75:25	1.1×10^{17}	7.1×10^{17}	film	CCD	···
z3409	21.31	50:50	1.3×10^{17}	9.1×10^{17}	film	CCD	···
z3462	20.81	50:50	8.0×10^{16}	9.3×10^{17}	CCD	CCD	···

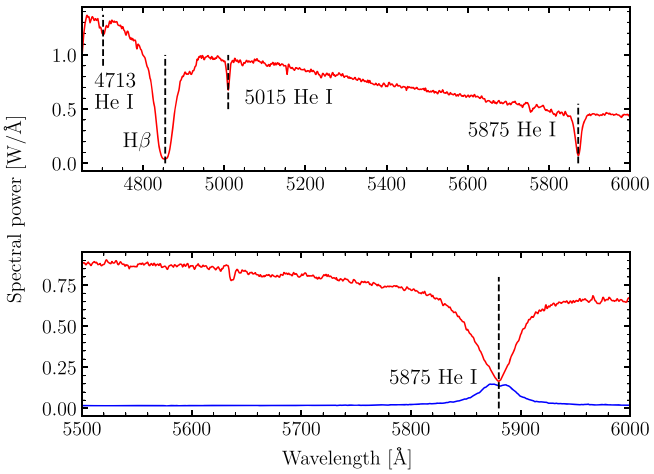

Figure 4. Sample spectra collected during a WDPE experiment. The top panel shows the Hβ and He5015 absorption data, while the bottom shows the He5875 emission and absorption features.

Figure 4 top panel are consistent with the plasma parameters presented in this paper and the gradients discussed in Schaeuble et al. (2019). The bottom panel of Figure 4 shows the emission and absorption data for He5875. More details about the spectrometer systems and other attributes of the data are discussed in Schaeuble et al. (2021). In Table 1, we list the diagnostic setups for each shot considered in this paper.

3. WDPE Data Extraction and Analysis Procedures

The data collected using the hardware and instruments described in Section 2 must be processed to extract all parameters needed for a benchmark line-shape experiment: plasma T_e, n_e, and $n_{neutral}$ values, as well as line-shape profiles. Each of these parameters must be extracted with uncertainties of $\leqslant$20%. The data extraction approach for these parameters is discussed in Sections 3.1 and 3.2. Benchmark theoretical line-shape validation tests also require an appropriate line-shape-fitting methodology and accurate instrumental broadening measurements, which are described in Section 3.3. The analysis associated with the He5875 data must be approached with special care, due to the unique data collection setup for that line. These effects are discussed in Section 3.4.

3.1. T_e, n_e, and $n_{neutral}$ Extraction Methods

We use Hβ to extract plasma n_e and T_e values needed for validating Stark broadening predictions. This transition is particularly suitable to serve as an n_e diagnostic, because it is well-studied in the WDPE platform. Falcon (2014) and Falcon et al. (2015) showed that four well-tested Hβ line-shape theories predict the same n_e values in the WDPE if plasma $n_e < 3 \times 10^{17}$ cm^{-3}. Schaeuble et al. (2019) demonstrated that potential plasma T_e and n_e gradients do not affect n_e values derived from Hβ. In the same publication, it was also shown that detailed line fits are not necessary to extract an accurate plasma n_e from Hβ. Full width at half area (FWHA) measurements of Hβ line profiles that have not been emission-corrected result in the same plasma n_e as line-shape fits to fully processed experimental data. We therefore adopt the FWHA n_e extraction approach here. As in Schaeuble et al. (2019), we use Xenomorph (Gomez et al. 2016; Cho et al. 2022) to translate our experimental FWHA values to plasma n_e. However, the choice of line-shape theory is ultimately unimportant for the present study, because Falcon et al (2015) showed that all major theories predict the same n_e at densities reached in the experiments presented here. The combination of the work presented in Falcon et al. (2015) and Schaeuble et al. (2019) gives us great confidence in the accuracy of the Hβ n_e values.

The Hβ n_e values are converted to a local thermodynamic equilibrium (LTE) temperature under the assumption that all electrons are being donated by H and that every neutral H atom is in the ground state (see Falcon et al. 2015). The resulting LTE temperatures are slight overestimates since our plasma is initially "overionized," leading to a larger than expected $n = 2$ population (e.g., Kawasaki et al. 2002). However, line shapes are much more sensitive to n_e and $n_{neutral}$, making T_e measurements of limited importance for the purposes of this paper.

The neutral densities ($n_{He\,I}$, $n_{H\,I}$) required for estimating the Van der Waals broadening contribution to the total measured line width are obtained through in situ gas pressure measurements (Schaeuble et al. 2021). The measured pressures in combination with the known gas composition allow for the derivation of n_{H_2} and n_{He} in the gas cell just prior to the experiment. The WDPE gas cell is repeatedly filled and purged before an experiment, to minimize the risk of gas contamination. The pressure data extraction procedure is described in Falcon (2014). The estimated pressure and particle density uncertainties are $\approx$1%. We convert the measured n_{H_2} and n_{He} to $n_{neutral}$ by assuming that all He stays neutral and that H donates all plasma e^-. This assumption is based on both experimental data and simulation results. We find no evidence of any He II lines in our experimental spectra. Further, all WDPE H/He mixture experiments are fielded at the same partial H pressure as the pure H experiments presented in Falcon et al. (2015) and Schaeuble et al. (2019). H/He experimental n_e values match those derived from pure H experiments, providing further evidence that He is not significantly ionized in the data presented in this paper. Finally, simulations of our plasma indicate that $\lesssim$10% of He is ionized at our plasma conditions. Subtracting n_e at every time step in the experiment from the measured n_H therefore results in $n_{neutral}$. n_e is constantly increasing as a function of time, $n_{H\,I}$ is always decreasing.

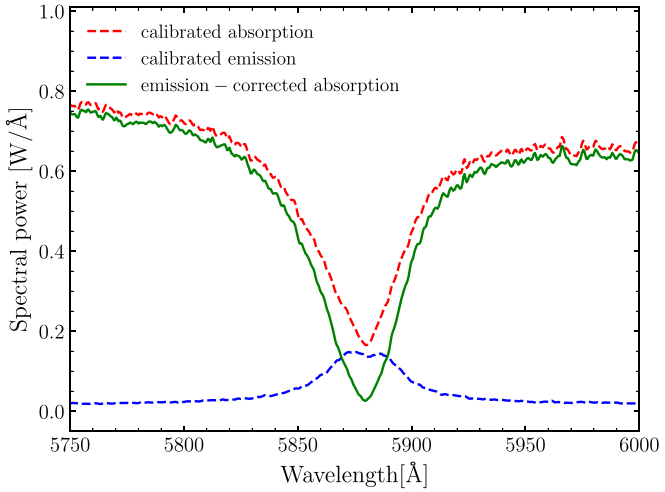

Figure 5. Comparison of calibrated absorption (red dashed), calibrated emission (blue dashed), and emission-corrected absorption (green) He5875 data collected on shot z3195. The plotted data is a 20 ns integration collected 40 ns after the onset of X-rays in the WDPE platform.

Adding the constant $n_{\mathrm{He\,I}}$ to the time-dependent $n_{\mathrm{H\,I}}$ then results in a n_{neutral} value at each time step in the experiment (see Figure 3). The U55 and D76 Van der Waals models predict that neutral hydrogen atoms provide more broadening than neutral helium. We add the predicted contributions in quadrature to arrive at the total width. Given our assumptions, the n_{neutral} values shown in Figure 3 might be lower estimates.

3.2. He5015 and He5875 Line-shape Extraction Methods

He5015 and He5875 WDPE line shapes are extracted for line-shape fitting using two separate methods. Since the He5015 is a weak line ($\tau \approx 0.3$) that shows little to no self-emission, this feature can be extracted by simply defining a continuum across the absorption line, converting it to transmission ($\mathbb{T}$), and then to optical depth ($\tau = -\ln(\mathbb{T})$). The optical depth of the He5875 line is much larger ($\tau \approx 5$) and exhibits significant self-emission (see Figure 4). More careful treatment is therefore required before extracting the line shape.

The data collected on the He5875 absorption LOS can be described as follows:

$$I_{\mathrm{abs}} = I_{\mathrm{backlighter}} \times \mathbb{T} + I_{\mathrm{self-emission}}, \quad (1)$$

where $I_{\mathrm{backlighter}}$ is the backlighter intensity and $I_{\mathrm{self-emission}}$ is the self-emission intensity along the LOS. Near the He5875 line center, $\mathbb{T}$ approaches zero, making the self-emission intensity a significant contributor to the recorded absorption signal. By subtracting the self-emission from the absorption data, we recover the true absorption that can be used to extract line-shape data. All He5875 data presented in this paper were calibrated using the process described in Schaeuble et al. (2021). The effect of the self-emission correction on the experimental He5875 profile can be seen in Figure 5, where we compare the calibrated absorption (red dashed) and emission (blue dashed) to the self-emission-corrected absorption (solid green). The green line is used for all He5875 analyses presented in this paper. Past studies have identified the incorrect/incomplete accounting for such self-emission/absorption effects as the most likely reason for faulty He5875 experimental measurements (e.g., Heading et al. 1992; Büscher et al. 1995). Cool boundary layer plasmas cause the observed emission–absorption line-shape discrepancy in Figure 5. These plasmas absorb from the center of each respective line shape. For emission, this results in a noticeable dip in the line-profile center, while the effect on absorption is much less noticeable.

3.3. Instrumental Broadening and Line-fitting Methods

Instrumental broadening measurements, the final ingredient needed to correctly fit experimental line shapes with calculations, are determined using a process outlined in Schaeuble et al. (2021). As described in that paper, we use laser lines to determine that the instrumental broadening of the CCD and film systems used in the WDPE has a Gaussian shape with FWHM of $\approx$6 Å. Recorded WDPE line shapes are broadened by both neutrals and charged particles in the plasma and the instruments used to record spectra. Theoretical line shapes only account for plasma processes. Instrumental effects must therefore be accounted for when fitting line shapes to experimental data.

Deconvolving the instrumental profile from the recorded spectra is a possibility, but numerically unstable and difficult. A much more straightforward approach is to convolve the theoretical line shapes with the instrumental profile during fitting, which is what we adopt for this paper. The convolution of the theoretical line shapes with the instrumental profile is performed in transmission (Schaeuble et al. 2019). The lowest WDPE FWHM measurements are comparable to the measured instrumental broadening (FWHM $\approx$ 6 Å; Schaeuble et al. 2021). Experimental line shapes are therefore significantly broadened by our data collection setup, and such effects need to be properly accounted for. See Schaeuble et al. (2021) for more details. The instrumental broadening convolved theoretical profiles are fit to experimental data using a Levenberg–Marquardt algorithm (Levenberg 1944; Marquardt 1963).

3.4. He5875 n_e Data Extraction Methodology

Special care is required when using Hβ to extract n_e values associated with He5875 line-shape data, because two separate LOS are used to collect each data set. As explained in Section 2, we capture both emission and absorption data for He5875. Absorption data captured on the CCD and film spectrometer systems are collected by arranging a fiber bundle containing two fibers side-by-side on the backlighter (see Figure 6). A top-to-bottom arrangement is not possible due to the geometric limitations of the backlighter. The adopted side-by-side arrangement results in one absorption LOS being closer to the gold back wall compared to the other. Since the gold wall is the main heating source in the WDPE gas cell, we expect the LOS closer to the gold wall to have a higher n_e compared to the one farther away. In the case presented in Figure 6, we expect the hi-res fiber to probe a higher n_e environment compared to the lo-res fiber.

Since the Hβ line is used to supply the n_e values needed to validate the He5875 line-profile calculations, we must ensure that the difference in probed plasma n_e is accounted for. Figure 7 shows the results of an experiment where Hβ was collected using the side-by-side arrangement shown in Figure 6. The blue curve in Figure 7 shows the Hβ n_e values for the LOS closer from the gold wall (hi-res fiber in Figure 6), while the red curve shows the Hβ n_e values for the LOS farther away (lo-res fiber in Figure 6). The data shown in that figure

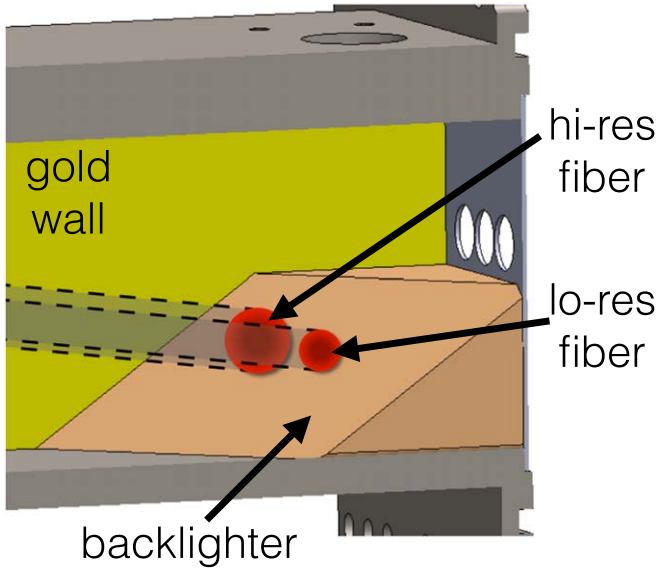

Figure 6. Detailed view of WDPE backlighter. Each absorption LOS as well as the gold back wall are identified in the figure.

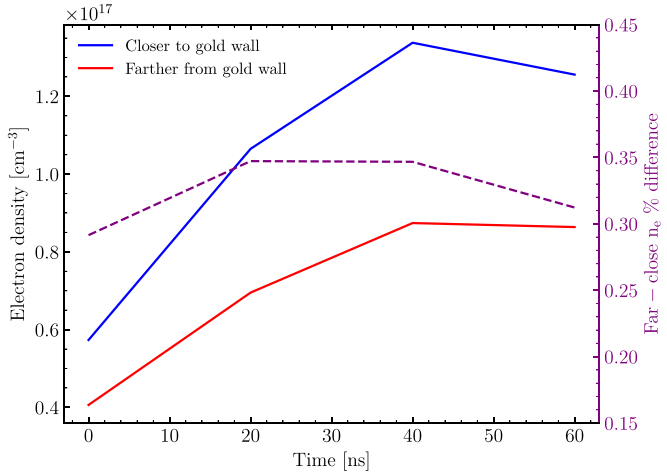

Figure 7. Comparison of Hβ n_e values as a function of time extracted from the same experiment (z3462), but using different LOS. Data depicted with the blue curve were collected closer to the gold wall and therefore exhibit higher Hβ n_e values, just as expected. Hβ n_e data collected on the farther LOS are plotted in red and show lower measurements. The difference between the two LOS is almost consistently ≈30%.

were collected on shot z3462. As expected, the LOS closer to the gold wall exhibits a higher n_e compared to that farther away. The n_e percent difference between the two LOS (dashed purple with purple right hand y-axis as reference) is very close to 30% for the entire duration of the experiment. We therefore apply this correction factor to the n_e values of all our He5875 experiments. While we only have a single data set in which we tracked the front–back alignment n_e differences, comparing the z3462 experimental results to other shots and applying the derived density differences to z3195 and z3402 produces consistent results across all shots, lending further credibility to this approach. For experiment z3195, the Hβ data were collected on the farther LOS and we therefore multiply the n_e values by 1.3 for line-shape validation. Experiment z3402 had the reverse setup, leading us to multiply its Hβ n_e values by 0.7.

4. Applicability of WDPE Plasma Conditions to DB Atmospheres

Performing meaningful Stark line-shape validation experiments for the problems associated with spectroscopic DB masses requires laboratory data collected at the T_e and n_e parameters found in He WD atmospheres where Stark broadening is thought to dominate. DB atmospheres span many orders of magnitude in n_e, and several factors in T_e. Identifying relevant plasma conditions at which to perform meaningful line-shape validation experiments is therefore challenging.

For modeling purposes, the astrophysical community generally considers atmospheres to be plane parallel and uses the Rosseland mean optical depth (τ_R) as a depth scale. τ_R is defined as $\sum_i \kappa_{R,i} \times l_i$ where κ_R is the Rosseland mean opacity and l is the length of layer i. Deeper atmospheric layers have higher τ_R, and also higher T_e, n_e, and $n_{neutral}$ values. The layer in which $\tau_\nu = 2/3$ (*not to be confused with* τ_R) is the so-called "line-forming" region in an atmosphere. Line cores will form at significantly lower τ_R values compared to continuum regions. This is caused by the additional opacity/optical depth provided by a line, which pushes the $\tau_\nu = 2/3$ point into lower τ_R regions (i.e., higher in the atmosphere). We define relevant DB atmosphere plasma conditions for this paper to be those found in the atmospheric layers where $\tau_\nu = 2/3$, or $\tau_R(\tau_\nu = 2/3)$. Layers with lower τ_ν may also contribute to the emergent stellar spectrum, but they have lower T_e and n_e values compared to the line-forming region. The relevant plasma conditions we list below are thus the highest T_e and n_e values expected to contribute to an emergent DB spectrum. We use the Montreal WD atmosphere models (Dufour et al. 2007; Bergeron et al. 2011) at standard DB conditions (T_{eff} = 17,500 K, $\log g$ = 8 cm s^{-2}, log(H/He) = −6; see Genest-Beaulieu & Bergeron 2019b) to predict plasma conditions in He WD line-forming regions. The log(H/He) parameter in a DB atmosphere model specifies the number abundance ratio of hydrogen to helium. A value of −6 indicates the presence of 1 hydrogen atom per 1 million helium atoms.

The $\tau_R(\tau_\nu = 2/3)$ structure and the corresponding T_e and n_e values for the He5015 and He5875 lines are plotted in Figure 8. The top panel in that figure identifies the atmospheric layer in which $\tau_\nu = 2/3$ (i.e., the line-forming region). We also identify the directions of the stellar surface and core in the top panel. Panels (B) and (C) show the n_e and T_e values found in the line-forming region. The WDPE n_e and T_e ranges are highlighted in gray in each panel. The atmospheric data shown in Figure 8 are only weakly dependent on $\log g$ and log(H/He).

The overlap between WDPE n_e and T_e ranges and the atmospheric conditions over which He5015 and He5875 are formed demonstrates the applicability of our data to investigating DB spectroscopic mass trends observed at 16,000 K $\lessapprox$ T_{eff} $\lessapprox$ 20,000 K. As evident from panel (B) of Figure 8, the WDPE achieves a slightly higher n_e compared to the line-forming regions found in DBs. However, the line-forming regions only constitute the visible part of an observed DB spectrum. Higher and lower atmospheric layers play an important role in the radiation transport and overall structure of a stellar atmospheres. Further, Stark broadening is more difficult to model at higher n_e, because the perturbation approximation fails, making validation at those n_e values more interesting (e.g., Falcon et al. 2015). WDPE T_e values agree well with DB atmospheric temperatures at which the He5015 and He5875 lines are formed.

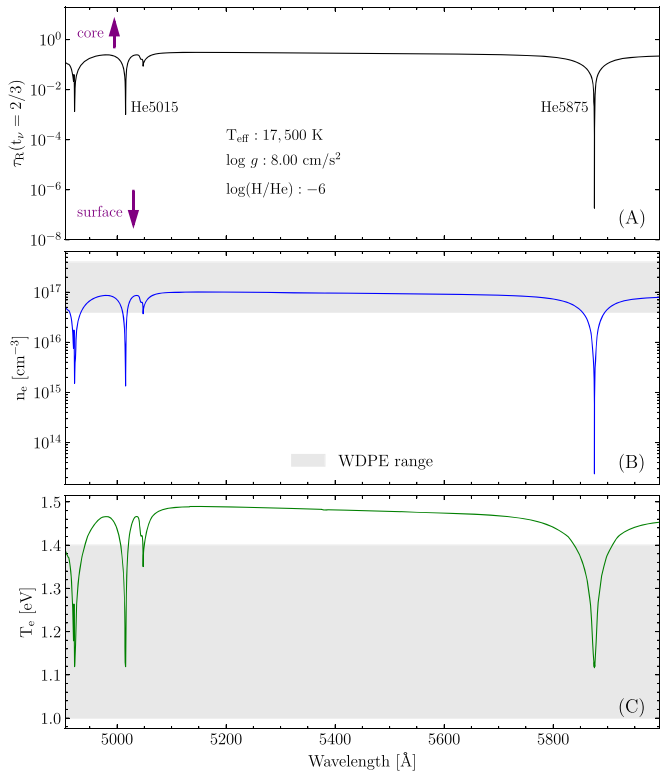

Figure 8. The top panel shows $\tau_R(\tau_\nu = 2/3)$ for DB atmosphere with $T_{eff} = 17{,}500$ K, log $g = 8$ cm s^{-2}, and log(H/He) $= -6$. Panels (B) and (C) give the n_e and T_e values corresponding to the layers plotted in panel (A). These plasma parameters are the highest n_e and T_e values to contribute to an emergent spectrum. WDPE experimental conditions are highlighted in gray.

5. Experimental Results

WDPE absorption and emission spectra represent a convolution of three different line-broadening mechanisms: instrumental, Stark, and Van der Waals. Section 3 describes how we incorporate instrumental broadening into our data analysis. The Stark and Van der Walls broadening models are examined simultaneously by comparing Hβ n_e to the n_e values inferred from line-profile fits to He5015 and He5875 using the B97 and our models (see Section 3). If these line-profile fits result in *higher* n_e values compared to Hβ, neutrals most likely contribute to the total observed line width. In this case, we deconvolve the Stark contribution predicted by models from the experimental line profile and ascribe the remaining broadening to Van der Waals processes. If the line-profile fits using the B97 or our models result in n_e values that are *lower* than or *match* the Hβ measurements, Van der Waals broadening is not important at WDPE plasma conditions. The U55 and D76 predictions indicate that, at $n_{neutral} \approx 1 \times 10^{18}$ cm^{-3} (WDPE maximum), the Van der Waals broadening contribution to the experimental line shape should be at least two orders of magnitude lower than Stark broadening contribution.

Since the main goal of our analysis is to investigate the accuracy of Stark He I line shapes used in the WD community to derive DB masses, we use the comparison between Hβ n_e and the line-shape-derived n_e as our validation metric, as opposed to the more traditional reduced χ^2 [6] value (e.g., Falcon et al. 2015). This approach has multiple benefits. First, comparing Hβ n_e to He n_e allows us to more directly assess the validity of spectroscopically determined DB masses. The χ^2_{red} metric would only show whether a theoretical line shape is a good match to experimental data. A line fit could have a $\chi^2_{red} \approx 1$, but still result in an incorrect n_e value. Second, using Hβ n_e and He I n_e differences allows more insightful study into potential systematic errors in the spectroscopic method. The numerical χ^2_{red} metric is of limited use in that respect. We therefore mainly analyze n_e trends in this section, but also calculate χ^2_{red} to elucidate differences between our Stark He line-shape calculations and B97.

We find that Hβ n_e and He n_e values agree well, indicating that observed He5015 and He5875 line widths can be explained using only Stark broadening. As predicted, Van der Waals processes are not needed to explain the data. We can therefore perform a full validation of the B97 and our Stark line-profile models. Careful examination of the He5015 data indicates that current Stark broadening theories may overestimate the FWHM of this line for a given n_e. Agreement between WDPE FWHM data and those presented in Chiang et al. (1977) further supports this conclusion.

5.1. Stark Broadening Results

We use WDPE He5015 and He5875 line-shape data to validate two Stark broadening line-shape theories: the semi-analytical B97 calculations (standard in WD community) and our computer-simulation-based Stark model. For this paper, the Stark energy level structure for our He I Stark calculations takes into account the state mixing effect due to the perturbing plasma electric microfield between all nonperturbed 1*snl* states with $n = 2$, 3, and 4. This leads to more accurate results for both line shifts and shapes compared to the former work presented in Gigosos et al. (2014)—where state mixing was only considered within the $n = 3$ manifold—and it also allows us to simultaneously obtain the calculations for all the involved line transitions at given plasma conditions from the same computer-simulation run. Furthermore, the new calculations include the so-called interference term between all transitions consistent with the improved energy level diagram. The experimental line shapes and the associated uncertainties presented in this section have been extracted according to the description given in Section 3 and Schaeuble et al. (2021).

Our validation procedure consists of two steps: first, we compare the n_e values resulting from the line-profile fits to the Hβ n_e values. Next, we determine how well theoretical line shapes match experimental data using χ^2_{red}. The first validation step is particularly important for this paper because it ensures that line-shape calculations can accurately predict n_e values, a vital ingredient in determining DB masses (see Section 1).

5.1.1. $3d \rightarrow 2p$ 5015 Å He I Results

We have four WDPE data sets that allow testing the B97 and our He5015 line-shape calculations: z3403, z3409, z3462_B, and z3462_F (see Table 1). The z3462 data sets were captured using the side-by-side backlighter alignment discussed in association with Figure 6. We denote the z3462 LOS closer to the gold back wall with "_B" (for back) and the one further away with "_F" (for front). All four data sets used for our He5015 investigation were collected using the CCD experimental setup described in Section 2.

[6] $\chi^2_{red} = \sum_i \left(\frac{\text{data}_i - \text{model}_i}{\sigma^2_{\text{data}}} \right)^2 \times \frac{1}{\text{deg. of freedom}}$

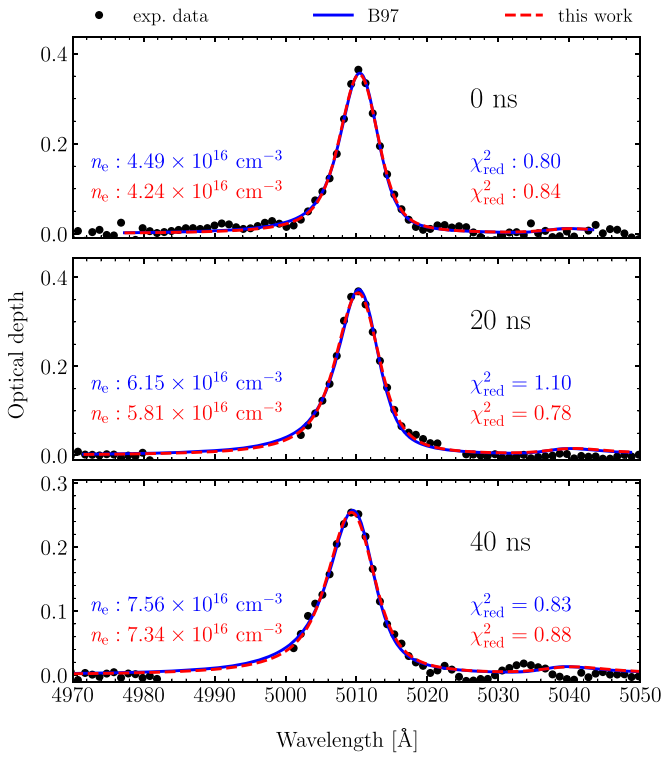

Figure 9. Sample fit of the B97 (solid blue) and our computer simulated (dashed red) line profiles to z3462_F He5015 data. The top, middle, and bottom panels, respectively, show the 0 ns, 20 ns, and 40 ns time steps. Each panel also lists n_e and the χ^2_{red} parameter for each fit.

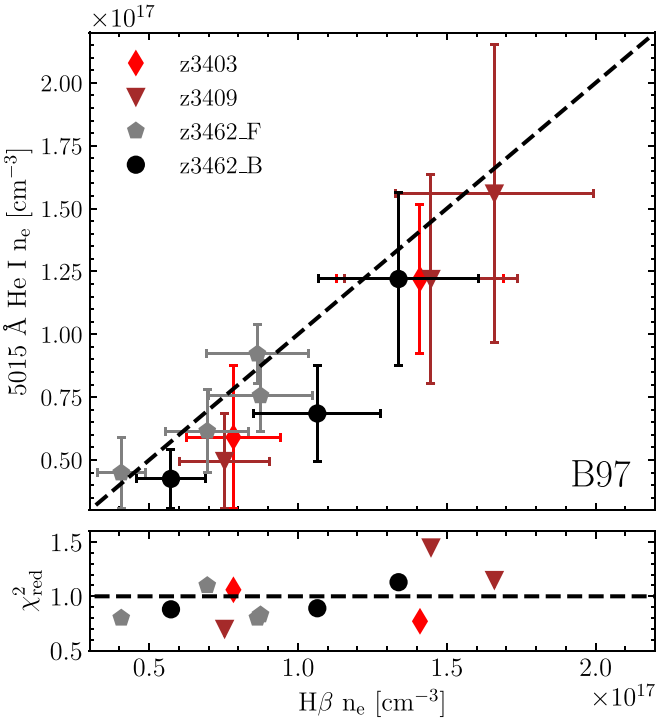

Figure 10. Top: Hβ n_e compared to n_e derived from fitting B97 line-shape models to WDPE experimental He5015 line data (see Figure 9). The Hβ n_e = He5015 n_e line is shown as a black dashed line. z3462_F and z3462_B refer to front and back data sets for this experiment. See Figure 7 and associated discussion for more details. Bottom: χ^2_{red} values for all data points shown in the top panel. All χ^2_{red} values $\lesssim$1, indicating good model–data fits.

Sample line-profile fits to z3462_F He5015 data are shown in Figure 9 for three time steps: 0 ns (top), 20 ns (middle), and 40 ns (bottom). Each time step represents a 20 ns integration, with the time given in each panel referencing the initial integration time (i.e., the 0 ns step integrates from 0 to 20 ns). The individual panels in Figure 9 show the experimental absorption data in optical depth units (black dots); the B97 (solid blue) and our (dashed red) line-profile fits (see Section 3.3). The N_e and χ^2_{red} values for each time step are also given in the panels. Here, $\chi^2_{red} \approx 1$, indicating a good fit with appropriately estimated uncertainties for each time step. No significant differences between the B97 and our own line profiles in either n_e or χ^2_{red} are apparent from the data presented in Figure 9. Fits to all other shots result in similar χ^2_{red} values and similarly good agreement between χ^2_{red} for B97 and our line profiles. We therefore conclude that both the B97 and our line-profile calculations reproduce the experimental data well and produce n_e values within 5%.

Hβ n_e values agree well with He5015 n_e values for the B97 and our line-shape calculations. Figure 10 shows this comparison for the B97 profiles, while Figure 11 depicts the Hβ–He5015 n_e plot for our calculations. The bottom panel of each figure shows the χ^2_{red} for each fit shown in the top panel. B97 line-shape fits to He5015 data result in n_e values that are ≈15 % lower than those derived from Hβ. For our line-shape calculations, the He5015 n_e values are, on average, 17% lower than those inferred from Hβ. Both the B97 and our theories therefore seem to overestimate line widths for a given plasma n_e.

To compare our experimental results to other experiments, we show a He5015 FWHM comparison as a function of n_e in

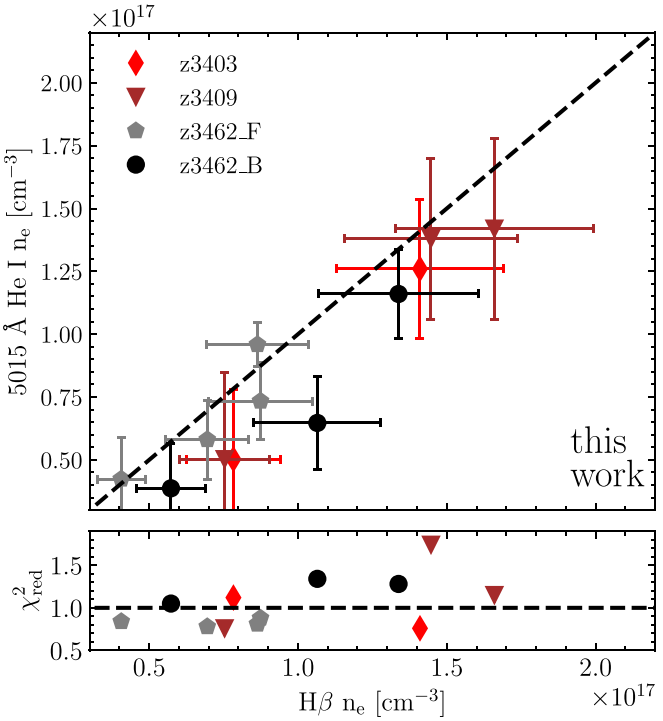

Figure 11. Top: Hβ n_e compared to n_e derived from fitting our line-shape models to WDPE experimental He5015 line data (see Figure 9). The Hβ n_e = He5015 n_e line is shown as a black dashed line. z3462_F and z3462_B refer to front and back data sets for this experiment. See Figure 7 and associated discussion for more details. Bottom: χ^2_{red} values for all data points shown in the top panel. All χ^2_{red} values $\lesssim$1, indicating good model–data fits.

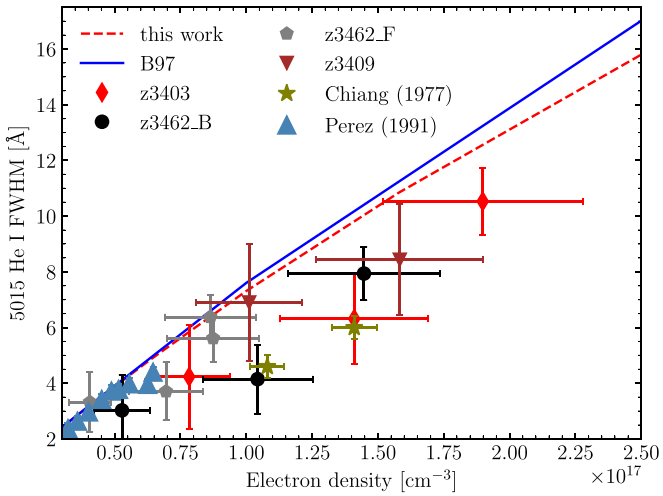

Figure 12. Comparison of FWHM-n_e data from previous experiments (Chiang et al. 1977; Perez et al. 1991) to WDPE measurements and predictions obtained from B97 (solid blue) and our own line-shape predictions (red dashed).

Figure 12. Other experiments (Chiang et al. 1977; Perez et al. 1991) only measured the FWHM, making this the only method of comparison. Data presented in Figure 12 demonstrate that, while our uncertainties are higher compared to other experiments, we still show the same line width trends. Furthermore, we also show the theoretical FWHM-n_e predictions of the B97 (solid blue) and our line shapes (red dashed). The agreement between other experiments, our experiments, and the theoretical predictions are good at lower densities ($n_e \lessapprox 1 \times 10^{17}$ cm^{-3}), but data collected at higher densities seem to indicate that both B97 and our line-shape theories may overpredict the FWHM at a given n_e. This mirrors trends observed in Figures 10 and 11.

He5015 n_e uncertainties shown in Figures 10 and 11 are derived by considering instrumental broadening, spectral line normalization, and CCD photon-counting uncertainties. Instrumental broadening uncertainties (see Schaeuble et al. 2021 for detailed derivation) are by far the largest contributor (>90%) to the final He5015 n_e error. This is not surprising, given that the instrumental broadening is comparable to the He5015 line width in the WDPE experiments. Small changes in the measured instrumental broadening will have measurable effects on the derived n_e value. Spectral line-normalization errors are the next-biggest contributor (≈10%) to the He5015 n_e uncertainty. The normalization contribution was derived by defining a continuum across the He5015 line in the WDPE data three times: (i) the ideal case, which we believe to be the true line-normalization continuum; (ii) the "upper" case, where the continuum was placed through the highest continuum data points available; and (iii) the "lower" case, during which the continuum was defined though the lowest continuum points. The He5015 line was renormalized with each continuum and fit with the B97 and our own line profiles. The resulting n_e values changed little as a result. The continuum placement test is particularly important for the He5015 line because it is located close to the red wing of the Hβ feature (see Figure 4). Defining an accurate continuum can therefore be challenging, especially at higher densities. Tests revealed that, despite the proximity of He5015 to Hβ, continuum placement does not introduce significant uncertainties into our analysis. If the continuum placement played an important role in our analysis, we expect the effects of this to be more severe at higher densities, given that the Hβ and He5015 lines are broader at those conditions, making accurate continuum placement more challenging due to line overlap. However, we see no such trends in Figures 9, 10, or 11. Taking the He5015 and Hβ n_e uncertainties into account and combining that with the information presented in Figures 10 and 11, we conclude that both the B97 and our He5015 line profiles are accurate within WDPE errors at the n_e conditions tested in our experiments.

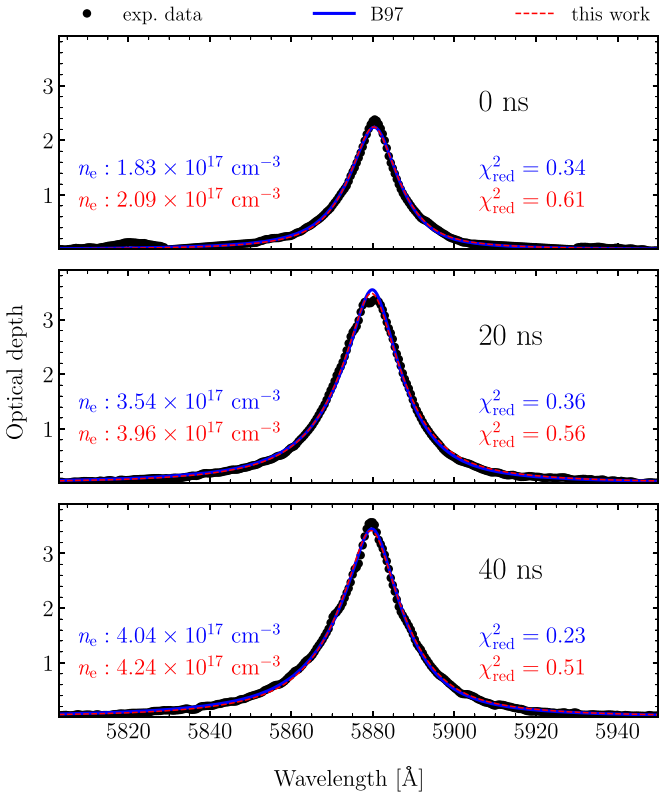

Figure 13. Sample fit of B97 (solid blue) and our He5875 line profiles (dashed red) to z3195 He5875 data. The top, middle, and bottom panels, respectively, show the 0 ns, 20 ns, and 40 ns time steps. Each panel also lists n_e and the χ^2_{red} parameter for each fit.

5.1.2. $3p \rightarrow 2s$ 5875 Å He I results

WDPE experiments z3195 and z3402 (see Table 1) are used to validate B97 and our He5875 line shapes. The experimental data for this transition is collected using three separate LOS: the low-resolution LOS captures the Hβ n_e diagnostic on film, and the two higher-resolution LOS capture the emission and absorption data on CCDs. Due to the high (≈8) optical depths and significant self-emission of this line at WDPE experimental conditions, the absorption data must be corrected for self-emission. A detailed description of this process and the associated errors are given in Schaeuble et al. (2021). Because Hβ and He5875 data are collected on separate LOS with two different distances from the gold back wall (see Figure 6 and Section 2), we have to adjust the Hβ n_e values accordingly (see Section 3.4). We remind the reader that these Hβ n_e adjustments are not performed to increase agreement between Hβ n_e and He5875 n_e values, but rather to account for the different plasma regions probed by the LOS.

Sample fits of B97 (solid blue) and our He5875 line profiles (dashed red) to z3195 He5875 data are shown in Figure 13. All these fits are performed to self-emission-corrected absorption data of shot z3195 (black dots). N_e and the χ^2_{red} parameters for each line-shape theory are also given in Figure 13. Each line-profile model appears to fit the data well. The $\chi^2_{red} < 1$ values

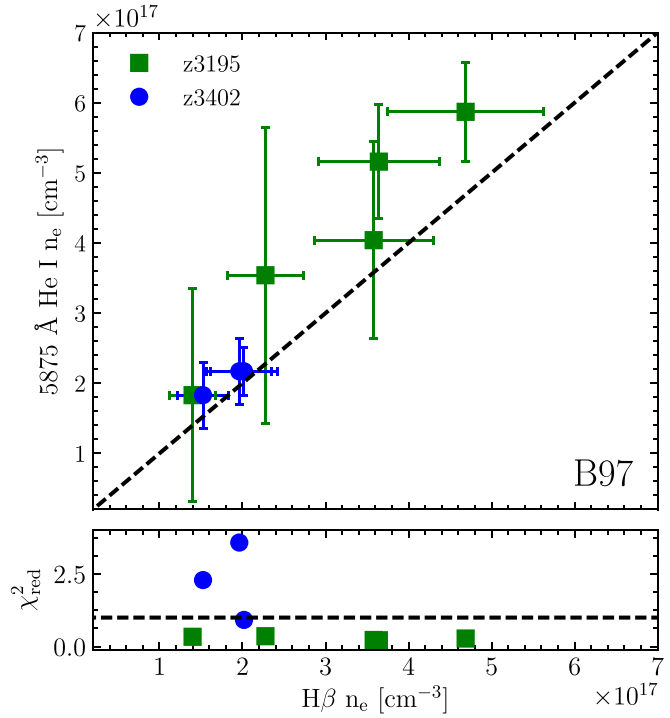

Figure 14. Top: Hβ n_e compared to n_e derived from fitting B97 line-shape models to WDPE experimental He5875 line data (see Figure 1). The Hβ n_e = He5875 n_e line is shown as a black dashed line. Bottom: χ^2_{red} values for all data points shown in the top panel. All χ^2_{red} values $\lessapprox$1, indicating good model–data fits.

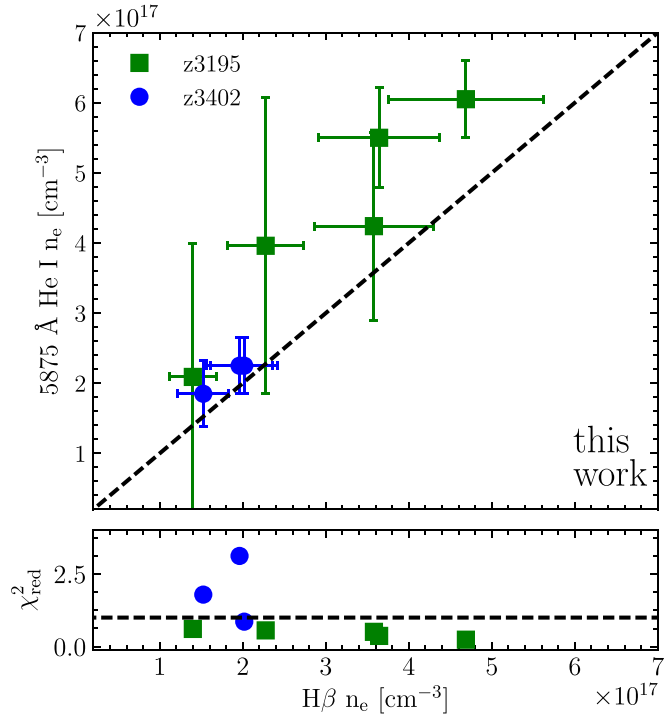

Figure 15. Top: Hβ n_e compared to n_e derived from fitting our line-shape models to WDPE experimental He5875 line data (see Figure 13). The Hβ n_e = He5875 n_e line is shown as a black dashed line. Bottom: χ^2_{red} values for all data points shown in the top panel. All χ^2_{red} values $\lessapprox$1, indicating good model–data fits.

indicate that we overestimated the errors for the line profiles. Uncertainties in the plotted profiles include contributions from photon-counting noise (≈2%) and uncertainty in the absolute scaling of the emission and absorption data sets (≈15%). As evident from Figure 5, the self-emission correction is most significant in the line core and has a negligible effect on the continuum. To estimate the total line-profile uncertainty, we thus adopt a value of 15% in the core and assign optical-depth-weighted uncertainties to the rest of the line profile, terminating with a 2% photon-counting error at the continuum.

Comparisons between Hβ n_e and He I n_e derived using B97 and our He5875 line-profile calculations are shown in Figures 14 and 15, respectively. The n_e equivalency line in those figures is plotted in dashed black. The bottom panel contains the χ^2_{red} values for each of the data points shown in the top panel. In contrast to the He5015 data shown in Figures 10 and 11, He5875 n_e values are higher than those derived from Hβ. On average, He5875 n_e values are 23% higher than Hβ n_e values for the B97 line shapes, and 28% higher for our own line shapes. These higher densities are largely driven by z3195. If only z3402 values are considered, the Hβ-He5875 n_e difference shrinks to 12% for B97 line shapes and 15% for our calculations.

Taken at face value, the χ^2_{red} shown in the bottom panel of Figures 14 and 15 suggest that the He5875 line-profile calculations do not reproduce the experimental data as accurately as the He5015 shown in Figures 10 and 11. This is particularly true for fits to z3402 that lead to χ^2_{red} of 2.29 and 3.58 for B97 and 1.79 and 3.12 for our profiles. Many factors influence the χ^2_{red} value, including the quality of fit between theory and experiment and the experimental uncertainties. As demonstrated in Figure 13, theoretical calculations fit well to experimental data. The measured χ^2_{red} values therefore indicate that experimental uncertainties are overestimated for z3195 and underestimated for z3402. These two data sets have different optical depths and different levels of self-emission, and are therefore subject to different systematic uncertainties. It is most likely these differences as well as inaccurate experimental uncertainties that are responsible for the χ^2_{red} discrepancies between z3195 and z3402. However, because the main purpose of this paper is to validate the predicted n_e of B97 and our own line shapes, we do not consider these χ^2_{red} discrepancies to be significant.

A comparison of our He5875 FWHM measurements to previous experiments as well as predictions by B97 and our own line shapes is shown in Figure 16. Just like with He5015, other He5875 experiments (Büscher et al. 1995; Milosavljević & Djeniže 2002) only measured FWHM values. Data presented in Figure 16 demonstrate that WDPE data again show the same trends as previous data and theoretical predictions. The agreement between other experiments, our experiments, and the theoretical predictions is excellent at lower densities ($n_e \lessapprox 2.5 \times 10^{17}$ cm^{-3}), but data collected at higher densities seems to indicate that both B97 and our line-shape theories may underpredict the FWHM at a given n_e. Similar trends are also observed in Figures 14 and 15.

The much larger (≈30%) He5875 n_e errors and elevated n_e values derived for z3195 compared to z3402 in Figures 14 and 15 can be traced back to significant differences in optical depths between the two experiments. The highest optical depth measured for z3195 is ≈10, while that for z3402 is only ≈5. This optical depth difference is most likely caused by the z3195 He5875 data being collected closer to the gold wall compared to z3402. A closer proximity to the gold wall results in more

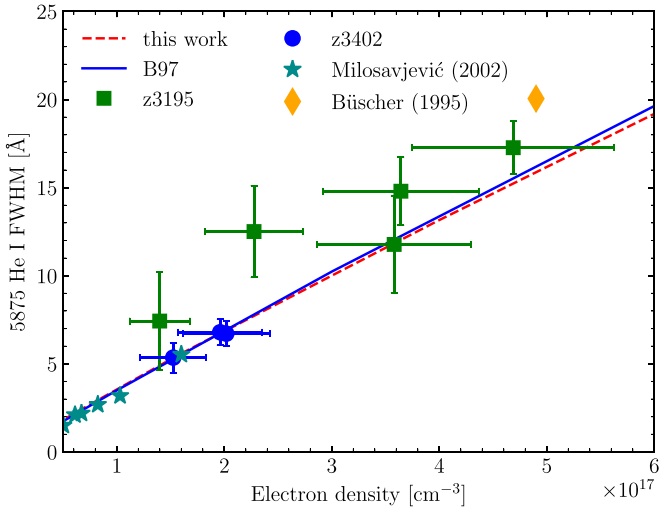

Figure 16. Comparison of FWHM collected during other experiments (Büscher et al. 1995; Milosavljević and Djeniže 2002) to WDPE data and predictions obtained from B97 (solid blue) and our own line-shape predictions (red dashed).

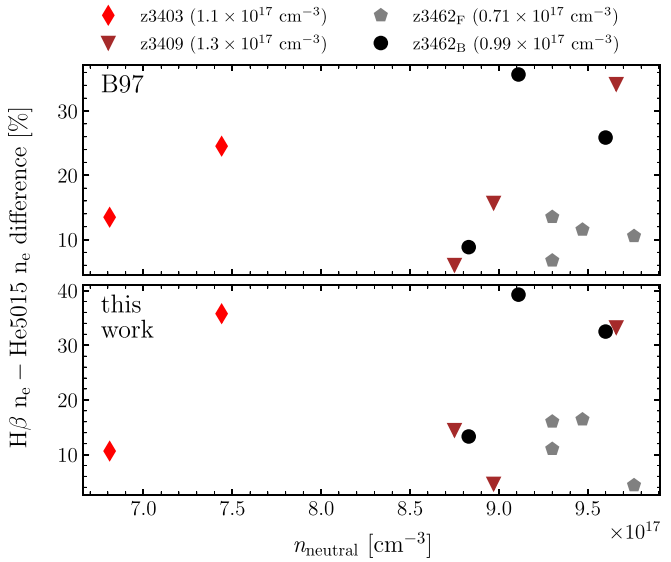

Figure 17. Top: Hβ–He5015 n_e percent differences plotted as a function of $n_{neutral}$ for B97 line-shape data. No trends are visible, indicating that Van der Waals broadening is not needed to explain measured line shapes. The average n_e for each shot is given in parentheses after the shot designation. Bottom: Same as top, but for our line shapes.

available photons to drive the 2*s* (He5875 lower level) populations and thus increase the optical depth of the line. As part of the fitting process, we convolve the line profile with the instrumental broadening. A line profile with a higher peak (as is the case for z3195 compared to z3402) will be more susceptible to changes in the measured instrumental broadening. At later times (higher n_e values), the measured line optical depth decreases, causing the measured instrumental broadening to have a smaller influence. The line is also wider at higher n_e values, leading to yet higher insensitivities regarding the measured instrumental broadening. We would therefore expect the He5875 n_e errors to decrease at higher n_e. This trend is confirmed by the z3195 data presented in Figures 14 and 15. We note here that the data presented in Figure 13 seem to indicate that the He5875 optical depth seems to slightly increase/stay constant with experiment time. However, the data shown in that figure are the *recorded* experimental profiles. To extract the true optical depth of the line, we must take instrumental broadening effects into account. Increases in experimental n_e result in broader He5875 lines, which means that instrumental effects become less important at higher densities. As a result, fitted optical depths decrease as a function of time. The larger optical depth for z3195 also put the line core close to the CCD detection limit. While there is no direct evidence that this line is saturated in our data, it would explain why the FWHM and n_e values measured for this line are higher than those for an experiment conducted at nominally the same conditions—z3402.

N_e uncertainties for each shot shown in Figures 14 and 15 were derived in a similar manner to the He5015 data presented in Figures 10 and 11, except that now the influence of the self-emission processes is also included. Just like with the He5015 data, instrumental broadening uncertainties dominate the errors shown in Figures 14 and 15. Self-emission correction uncertainties, including the relative scaling and shift of the emission and absorption spectra during the correction process, have a negligible effect (<10%) on the He5875 n_e value. The He5875 line is isolated in our spectrum (see Figure 4), which allows for easier continuum definition compared to the He5015 data. Continuum normalization errors also have a negligible effect on the final line shape and n_e. CCD photon-counting uncertainties are also negligible for the He5875 line.

5.2. Van der Waals Broadening Contributions

The data presented in Figures 10, 11, 14, and 15 strongly suggest that, despite a significant and varying neutral density in the WDPE plasma, Van der Waals broadening does not need to be invoked to explain our experimental results. At the maximum WDPE neutral densities ($n_{neutral} \approx 1 \times 10^{18}$ cm^{-3}), both the U55 and D76 Van der Waals broadening theories predict negligible broadening for H I and He I, making this result not entirely unsurprising.

Our conclusions regarding Van der Waals broadening are confirmed by the He5015 data. The experiments presented in Figures 10 and 11 do not show a need to invoke any Van der Waals broadening models to explain any n_e disagreements between Hβ and He5015. In fact, current Stark broadening theories seem to slightly overestimate the line width for a given n_e value. If Stark broadening was not sufficient to fully explain experimental data, we would expect an increased influence at lower Hβ n_e values, given that $n_{neutral}$ is highest at that time. Figure 17 depicts the n_e percent difference between Hβ and He5015, plotted as a function of experimental $n_{neutral}$. If Van der Waals broadening were important, we would expect to see a positive correlation between the plotted parameters. No such correlation is observed. The upper panel shows the results for B97, while the lower panel shows our line-shape trends. We include the average n_e of each plotted experiment in the legend.

He5875 FWHM and n_e measurements also do not necessitate any Van der Waals broadening. Figure 18 shows Hβ–He5875 n_e percent differences as a function of $n_{neutral}$, and again no obvious trends are observed. Shots z3195 and z3402 (see Figures 14 and 15) contained $\approx 7 \times 10^{17}$ cm^{-3} neutral helium atoms. Potential reasons for why z3195 FWHM and n_e measurements are higher than those for z3402 are discussed in Section 5.1.2. We do not attribute these differences to Van der

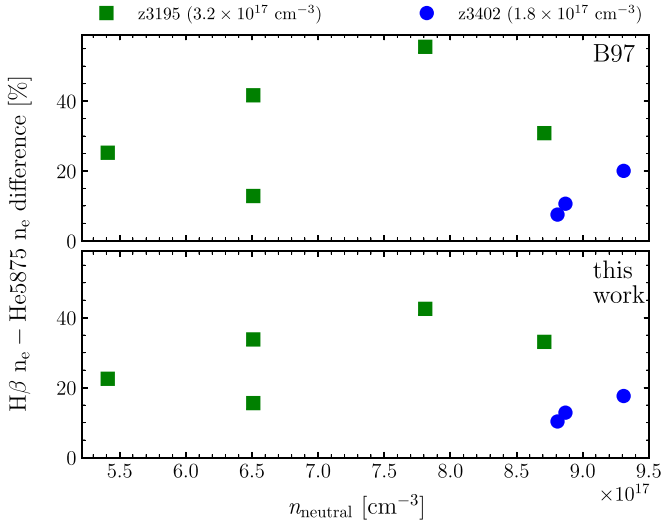

Figure 18. Top: Hβ–He5875 n_e percent differences plotted as a function of $n_{neutral}$ for B97 line-shape data. No trends are visible, indicating that Van der Waals broadening is not needed to explain measured line shapes. The average n_e for each shot is given in parentheses after the shot designation. Bottom: Same as top, but for our line shapes.

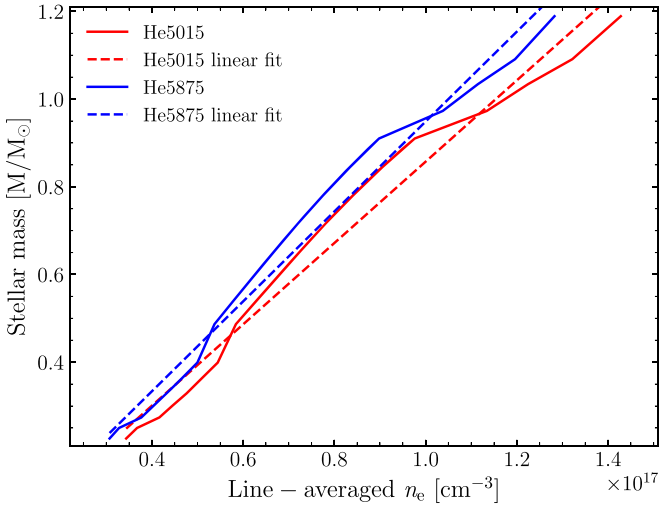

Figure 19. Relationship between line-formation averaged n_e and stellar mass for the He5015 (red) and He5875 (blue). We also show the linear fits to these relationships as dashed lines. The slopes of these linear fits (d(mass)/$d(n_e)$) allow us to estimate how n_e uncertainties in our data affect derived spectroscopic DB masses.

Waals broadening. Figure 18 shows trends similar to those in Figure 17, leading to the same conclusions.

5.3. Relating Experimental n_e Uncertainties to Spectroscopic-Photometric DB Mass Differences

Drawing astrophysically meaningful conclusions using our experimental results requires understanding the relationship between our experimental He I n_e uncertainties, DB atmospheric n_e values, and the corresponding stellar mass. Because both lines under investigation in this paper form over large n_e ranges in DB atmospheres (see panel (B) in Figure 8), it is difficult to develop a comprehensive understanding of this relationship without performing detailed fits to DB observations that take our experimental line-shape and n_e uncertainties into account. Such a study is beyond the scope of this paper.

To derive an approximate atmospheric n_e–stellar mass relationship, we calculate the average n_e value over which the He5015 and He5875 lines are formed at a given $\log g$ and T_{eff} using the same data as plotted in Figure 8 and relate the results to stellar mass. For He5875, we average over all n_e within 125 Å of line center in Figure 8, while He5015 line-forming n_e is calculated by averaging all n_e values within 25 Å of line center. We vary $\log g$ from 7.0 to 9.0 in 0.1 step increments and set $T_{eff} = 17{,}500$ K for the purposes of this test. The $\log g$ and T_{eff} combinations are converted to a stellar mass using the Montreal White Dwarf Database[7] (Dufour et al. 2017). The results in Figure 19 show the resulting DB line-forming n_e–mass relationship for both He5015 (red) and He5875 (blue). As outlined in the discussion accompanying Figure 8, the WDPE reaches higher n_e as compared to DB atmospheric line-forming regions. This is again reflected in Figure 19. However, we are only interested in deriving the *change* in mass as a function of the *change* in n_e for the purposes of this test (i.e., d(mass)/$d(n_e)$). Since both of the presented mass–n_e relationships are nearly linear, we use the slope of the linear fits to quantify the mass uncertainty associated with our experimental He I n_e uncertainty. The slope is independent of overall n_e, limiting the significance of the small mismatch between experimental and DB line-forming n_e.

The derived DB atmospheric n_e–stellar mass trends reveal a roughly one-to-one relationship between mass and atmospheric n_e. Hence, our experimental He I n_e uncertainties approximately correspond to DB mass uncertainties. The shots with the lowest He I n_e uncertainties are z3402 for He5875 and z3462_F, both of which have data points with a ≈10% uncertainty, implying a 10% DB mass uncertainty. This is smaller than the ≈20% mass difference between spectroscopic and photometric masses at 16,000 K $\lessapprox T_{eff} \lessapprox$ 20,000 K. Other experiments presented in this paper have larger He I n_e uncertainties, but all presented data sets are internally consistent and agree with other experimental data (see Figures 12 and 16). Therefore, repeating these experiments with a platform that results in lower uncertainties would be unlikely to change these conclusions. It is important to note, however, that the approach presented here is only an estimate of the atmospheric n_e–stellar mass relationship. A fully integrated test, where many detailed DB fits that incorporate all our experimental uncertainties (n_e, line shape, etc.) are performed, is needed to solidify these conclusions.

6. Conclusions

In this paper, we present experimental data to validate line-shape calculations for the He5015 and He5875 lines using two separate theories: the semi-analytical B97 and our computer-simulation-based He I Stark line shapes. The U55 and D76 Van der Waals theories predict negligible neutral broadening at WDPE conditions, which we confirm with our experimental data. The B97 theory is the standard in the WD community, and spectroscopically derived DB masses are thought to be dependent on their accuracy.

Our results show that Stark He5015 and He5875 line-shape theories (B97 and our theory) are accurate at n_e values found in DB atmospheres. Furthermore, our experimental uncertainties indicate that differences between spectroscopic and photometric masses most likely cannot be attributed solely to Stark

[7] https://www.montrealwhitedwarfdatabase.org/

line-profile deficiencies, if at all. These conclusions are supported by the data presented in Figures 10–16, as well as the discussion in Section 5.3. Determining other spectroscopic input parameters that could potentially be responsible for the observed DB spectroscopic-photometric mass disagreements is difficult because this mass determination process is nuanced, complicated, and reliant on many assumptions (Cukanovaite et al. 2021). Many different parameter choices contribute to a final spectroscopic DB mass. However, applying B97 line shapes to DB spectroscopic mass determination studies at $T_{\rm eff} > 16{,}000$ K should produce masses that are more accurate than the current disagreement between photometry and spectroscopy (Genest-Beaulieu & Bergeron 2019a, 2019b; Tremblay & Cukanovaite 2019).

The U55 and D76 Van der Waals broadening predictions were also shown to be accurate at $n_{\rm neutral}$ conditions tested in this paper. This allows us to draw some astrophysically meaningful conclusions from our data. First, at $T_{\rm eff} \gtrapprox 15{,}000$ K, neutral broadening does not affect the He5015 or He5875 lines, just as predicted by theory. To ascertain the true effect of neutral broadening on the apparent DB mass upturn at $T_{\rm eff} < 16{,}000$ K, it may be interesting to only fit line cores of He5875 and other strong lines. If Van der Waals broadening is truly the cause of the observed increase in scatter, such fits should result in spectroscopic masses whose scatter matches that found at $T_{\rm eff} > 16{,}000$ K. Our Stark broadening validation data seems to suggest that other effects, which are not yet well-understood, could potentially be causing spectroscopic mass determination problems. Weaker lines such as He5015 are formed over much less severe $n_{\rm e}$, $n_{\rm neutral}$, and $T_{\rm e}$ gradients in a DB atmosphere. Fitting their line cores should therefore not result in significant mass differences when compared to a whole-line fit.

More work remains to be done to fully investigate and explore remaining DB spectroscopic mass issues. The most immediate need is for Van der Waals measurements at $n_{\rm neutral}$ conditions found in lower-temperature DBs. Modest experimental changes should allow us to achieve this goal. Further, more He I lines should be validated so that more concrete conclusions can be drawn with regards to still unexplained spectroscopic mass trends. All these issues will be addressed in a future publication.

This work was performed at Sandia National Laboratories. We thank the Z-facility teams, and in particular, G. Loisel, D. Scogiletti, S. Patel, D. Begay, D. Bliss, A. York, J. Hanson, and K. MacRunnels for their support. We thank P. Tremblay and P. Bergeron from the Université de Montréal for sharing the B97 line profiles with us. We also thank Alan Wootton and Greg Rochau for championing our fundamental science research efforts. M.S., B.D., M.H.M., and D.E.W. acknowledge support from the Wootton Center for Astrophysical Plasma Properties under the United States Department of Energy collaborative agreement DE-FOA-0001634, from the United States Department of Energy grant under DE-SC0010623, and from the National Science Foundation grant under AST 1707419. M.A.G. and R.F. have been supported by the Research grant No. CEI2020-FEI02 from the Consejería de Economía, Industria, Comercio y Conocimiento del Gobierno de Canarias; and by Research grant No. PID2019-108764RB-I00 from the Spanish Ministry of Science and Innovation. Sandia National Laboratories is a multi-mission laboratory managed and operated by National Technology and Engineering Solutions of Sandia, LLC., a wholly owned subsidiary of Honeywell International, Inc., for the U.S. Department of Energy's National Nuclear Security Administration under contract DE-NA-0003525. This paper describes objective technical results and analysis. Any subjective views or opinions that might be expressed in the paper do not necessarily represent the views of the U.S. Department of Energy or the United States Government.

ORCID iDs

M.-A. Schaeuble https://orcid.org/0000-0001-8869-5203
S. Blouin https://orcid.org/0000-0002-9632-1436
B. Dunlap https://orcid.org/0000-0002-1086-8685
M. H. Montgomery https://orcid.org/0000-0002-6748-1748
D. E. Winget https://orcid.org/0000-0003-0181-2521

References

Bailey, J. E., Chandler, G. A., Mancini, R. C., et al. 2006, PhPl, 13, 056301
Beauchamp, A., Wesemael, F., & Bergeron, P. 1997, ApJS, 108, 559
Bergeron, P. 1993, White Dwarfs: Advances in Observation and Theory, Vol. 403 (Leicester: Kluwer Academic Publishers), 267
Bergeron, P., Wesemael, F., Dufour, P., et al. 2011, ApJ, 737, 28
Büscher, S., Glenzer, S., Wrubel, T., & Kunze, H.-J. 1995, JQSRT, 54, 73
Chiang, W. T., Murphy, D. P., Chen, Y. G., & Griem, H. R. 1977, ZNatA, 32, 818
Cho, P. B., Gomez, T. A., Montgomery, M. H., et al. 2022, ApJ, 927, 70
Choi, J., Dotter, A., Conroy, C., et al. 2016, ApJ, 823, 102
Cukanovaite, E., Tremblay, P.-E., Bergeron, P., et al. 2021, MNRAS, 501, 5274
Cummings, J. D., Kalirai, J. S., Tremblay, P.-E., et al. 2018, ApJ, 866, 21
Deridder, G., & van Renspergen, W. 1976, A&AS, 23, 147
Dufour, P., Bergeron, P., Liebert, J., et al. 2007, ApJ, 663, 1291
Dufour, P., Blouin, S., Coutu, S., et al. 2017, in 20th European White Dwarf Workshop, ed. P.-E. Tremblay et al. (San Francisco, CA: ASP)
Dufour, P., Fontaine, G., Liebert, J., Schmidt, G. D., & Behara, N. 2008, ApJ, 683, 978
Falcon, R. E. 2014, PhD, University of Texas at Austin
Falcon, R. E., Rochau, G. A., Bailey, J. E., et al. 2013, HEDP, 9, 82
Falcon, R. E., Rochau, G. A., Bailey, J. E., et al. 2015, ApJ, 806, 214
Fontaine, G., & Wesemael, F. 1987, in Proc. IAU Coll. 95 (Schenectady, NY: David Press), 319
Genest-Beaulieu, C., & Bergeron, P. 2019a, ApJ, 871, 169
Genest-Beaulieu, C., & Bergeron, P. 2019b, ApJ, 882, 106
Gigosos, M. A., Djurović, S., Savic, I., et al. 2014, A&A, 561, A135
Gomez, T. A., Nagayama, T., Kilcrease, D. P., et al. 2016, PhRvA, 94, 022501
Heading, D. J., Marangos, J. P., & Burgess, D. D. 1992, JPhB, 25, 4745
Jones, M. C., Ampleford, D. J., Cuneo, M. E., et al. 2014, RSciI, 85, 083501
Kawasaki, M. T., Ozaki, M., Nagase, F., et al. 2002, ApJ, 572, 897
Koester, D., & Kepler, S. O. 2015, A&A, 583, A86
Levenberg, K. 1944, QApMa, 2, 164
Marquardt, D. W. 1963, J. Soc. Ind. Appl. Math., 11, 431
McDaniel, D. H., Mazarakis, M. G., Bliss, D. E., et al. 2002, in AIP Conf. Proc. 651, Dense Z-Pinches: 5th Int. Conf. on Dense Z-Pinches (New York: AIP), 23
Milosavljević, V., & Djeniže, S. 2002, A&A, 393, 721
Nather, R. E., Robinson, E. L., & Stover, R. J. 1981, ApJ, 244, 269
Perez, C., de La Rosa, I., de Frutos, A. M., & Mar, S. 1991, PhRvA, 44, 6785
Rochau, G. A., Bailey, J. E., Falcon, R. E., et al. 2014, PhPl, 21, 056308
Rose, D. V., Welch, D. R., Madrid, E. A., et al. 2010, PhRvS, 13, 010402
Schaeuble, M.-A., Nagayama, T., Bailey, J. E., et al. 2019, ApJ, 885, 86
Schaeuble, M. A., Nagayama, T., Bailey, J. E., et al. 2021, PhPl, 28, 062902
Sinars, D. B., Sweeney, M. A., Alexander, C. S., et al. 2020, PoP, 27, 070501
Sion, E. M., Greenstein, J. L., Landstreet, J. D., et al. 1983, ApJ, 269, 253
Tremblay, P., Beauchamp, A., & Bergeron, P. 2020, ApJ, 901, 104
Tremblay, P. E., & Cukanovaite, E. 2019, MNRAS, 482, 5222
Tremblay, P.-E., Ludwig, H.-G., Steffen, M., & Freytag, B. 2013, A&A, 559, A104
Unsold, A. 1955, Physik der Sternatmospharen, MIT besonderer Berucksichtigung der Sonne (Berlin: Springer)
Werner, K., & Herwig, F. 2006, PASP, 118, 183